Water Resources Research

RESEARCH ARTICLE

10.1029/2025WR041274

Inertial Effects on Fluid Flow Through Natural Porous Media

Sahrish B. Naqvi[1], Damian Śnieżek[1], Dawid Strzelczyk[1,2], Mariusz Mądrala, and Maciej Matyka[1,2]

[1]Faculty of Physics and Astronomy, Institute of Theoretical Physics, University of Wrocław, Wrocław, Poland, [2]Institute Jožef Stefan, Ljubljana, Slovenia

Key Points:

- We investigate inertial effects in the pore-space fluid flow through natural porous media at varying Reynolds number
- Tortuosity and energy distribution change with the structure of the flow in the microscale (vortex formation and identification)
- We find scaling law for apparent permeability-tortuosity relation in the inertial regime (numerical study)

Correspondence to:

M. Matyka,
maciej.matyka@uwr.edu.pl

Citation:

Naqvi, S. B., Śnieżek, D., Strzelczyk, D., Mądrala, M., & Matyka, M. (2026). Inertial effects on fluid flow through natural porous media. *Water Resources Research*, *62*, e2025WR041274. https://doi.org/10.1029/2025WR041274

Received 9 JUN 2025
Accepted 5 DEC 2025

Author Contributions:

Conceptualization: Mariusz Mądrala, Maciej Matyka
Data curation: Damian Śnieżek, Mariusz Mądrala
Formal analysis: Sahrish B. Naqvi, Damian Śnieżek, Dawid Strzelczyk, Maciej Matyka
Funding acquisition: Maciej Matyka
Investigation: Sahrish B. Naqvi, Maciej Matyka
Methodology: Sahrish B. Naqvi, Maciej Matyka
Project administration: Maciej Matyka
Resources: Mariusz Mądrala, Maciej Matyka
Software: Sahrish B. Naqvi
Supervision: Maciej Matyka
Validation: Sahrish B. Naqvi
Visualization: Sahrish B. Naqvi
Writing – original draft: Sahrish B. Naqvi, Mariusz Mądrala, Maciej Matyka
Writing – review & editing: Sahrish B. Naqvi, Damian Śnieżek,

Abstract

We investigated the nonlinear effects of gravity-driven fluid flow through a two-dimensional, moderately low-porosity, packed bed of stubby stone grains in Darcy, and post Darcy regimes. We focused on preferential channel formation, tortuosity, spatial distribution of kinetic energy, and vortex formation. We show that nonlinear effects dominate at relatively high Reynolds numbers, even though the deviation from Darcy's law is not visible in friction factor measurements. A backward-flow fraction ρ^{-} captures the earliest formation and growth of recirculation zones; the participation number π increases monotonically, indicating a progressive delocalization of kinetic energy; and tortuosity τ exhibits a non-monotonous trend—initially flat/slightly decreasing, then rising in the inertial regime. The apparent permeability decreases with Re. These results explain why friction-factor-only indicator can obscure the onset of inertial effects in the real porous rocks with moderate porosity, lower than of those studied previously and identify ρ^{-} as an early, robust indicator of recirculation. We further notice an increased asymmetry of the flow field revealed by vorticity analysis and surprising correlation between tortuosity and apparent permeability in the inertial flow regime, where the relation $\kappa_{\mathrm{app}} \propto \tau^{-1/3}$ holds.

Plain Language Summary

Understanding the mechanisms of variation in the speed and trajectories of water particles in the pore medium is essential for optimizing water exploitation and contaminant migration in the aquifer. In most of the water flow models considered, the geometry of the pore medium dictates a relatively slow, laminar flow. However, at higher water velocities, the fluid flow quickly becomes non-linear. In this study, we used an artificially prepared sample of pore medium grains and utilized numerical simulations to see how the flow pattern changes as the driving force increases through this medium following narrow, tortuous pathways between the grains. We show that, in a porous medium, narrow zones of reverse flow and recirculation appear very early and grow into a complex network of vortices at higher flow rates. Quantities that describe how tortuous the flow paths are, how fast the fluid flows through the pore space, and how often the fluid reverses direction show clear and strong shifts as the flow speeds increase. Meanwhile, the standard friction-based indicator hardly changes at all. These results provide practical pore-scale indicators of the onset of inertial flow that can help improve predictions for groundwater management, CO_2 storage, and hydrocarbon production.

1. Introduction

Fluids, when flowing through porous media, form self-organized, preferential flow channels, which under high driving forces may be affected by inertial effects emerging at high Reynolds numbers (Andrade Jr et al., 1999; Matyka & Mądrala, 2017; Nissan & Berkowitz, 2018; Śnieżek et al., 2024). The dynamic interaction of the viscous fluid with the microstructure of the porous medium shapes preferential paths (Hyman, 2020). In a low-porosity medium, the fluid navigates through narrow tortuous pathways that follow the geometry of the pore space. The channeling effects are enhanced at low Reynolds number conditions, which may hinder the visibility of inertial effects in experiments (Wang et al., 2019). Understanding the mechanisms governing flow channelization in low-porosity media is essential across various domains including subsurface energy storage, CO_2 sequestration, and low-permeability reservoir engineering (Hovorka et al., 2019). Low-porosity porous media are fundamental to various engineering applications, such as microfluidic device design (Cao et al., 2019), advanced energy systems (Banerjee & Paul, 2021), high-efficiency filtration technologies (Zhang et al., 2024), and thermally active catalytic reactors (Wang et al., 2014), where constrained pore networks influence transport and reaction processes.

Traditionally, two models have been used to describe the flow through porous materials. Originally, they were formulated as empirical laws (Darcy, 1856; Forchheimer, 1901) and were later derived theoretically on the basis

Dawid Strzelczyk, Mariusz Mądrala, Maciej Matyka

of upscaling of the solution of the pore-scale fluid flow equations. In the laminar low-velocity regime, the Darcy law establishes a linear relationship between the forcing term and flow velocity:

$$\mathbf{U} = \frac{\kappa}{\mu}\mathbf{f}, \tag{1}$$

where **U** is the superficial velocity, μ is the dynamic viscosity of the fluid, κ is the medium's permeability, L is the domain length, and **f** the body force (Neuman, 1977; Whitaker, 1986). However, deviations from linearity are observed as the fluid velocity increases, and the inertial effects become significant. Thus, second-order correction is often introduced in the form of the Forchheimer equation:

$$\mathbf{U} = \frac{\kappa}{\mu}\mathbf{f} - \beta\rho\kappa^{1/2}|\mathbf{U}|\mathbf{U}, \tag{2}$$

where β is an empirical inertial coefficient (Arbabi & Sahimi, 2024; Basak, 1977; Whitaker, 1996; Zeng & Grigg, 2006). The onset and strength of inertial transition depend sensitively on both the magnitude and spatial distribution of medium properties (e.g., porosity), that is, on a particular form of heterogeneity (Fourar et al., 2005). An increase in the driving forces governs the transition from the linear Darcy regime to the inertial flow, which comprises many physical phenomena. In particular, as the Reynolds number (Re) increases, local flow separation is observed with vortex formation and enhanced drag, resulting in the quadratic correction term in Equation 2 (Whitaker, 1996; Zeng & Grigg, 2006). However, experimental studies have demonstrated that at very low Reynolds numbers, the flow may deviate from the linear behavior predicted by the Darcy law, commonly referred to as the pre-Darcy regime, where the pressure–velocity relationship becomes nonlinear even in the absence of inertial effects (Wang et al., 2019). Numerical simulations further support that the porosity is a decisive factor in determining the critical transition point to nonlinearity (Arbabi & Sahimi, 2024). For example, pore-scale simulations of bead-packs, Bentheimer sandstone, and Estaillades carbonate indicate that despite having similar porosities, heterogeneous rocks such as Estaillades exhibit the onset of inertial flow at Reynolds numbers two to three orders of magnitude lower than in homogeneous media (Muljadi et al., 2015, 2016). These differences are attributed to the influence of the pore geometry and the formation of steady vortices that appear along with changes in the velocity distribution in the pore space.

In a highly porous medium, the fluid gains momentum easily, enabling the early onset of nonlinearity and pronounced inertial effects (Andrade Jr et al., 1999). However, these observations primarily stem from idealized or high-porosity systems. Natural porous materials, particularly those with low porosity, exhibit more intricate geometries of the pore space, where the structural heterogeneity and geometric tortuosity of pores play a dominant role and lead to vortex formation even at low Reynolds numbers. Our understanding of the low-porous medium is that it exhibits complex flow paths driven mainly by geometry. They are highly resistant, which weakens the inertial effects in flow (Arthur, 2020). Thus, the physical mechanism of inertia and transition to nonlinearity is much more complicated than in a highly porous medium reported in (Andrade Jr et al., 1999; Śnieżek et al., 2024).

We aim to investigate real, low-porosity geological rock sample to understand better the transition from a linear to a nonlinear regime with increasing Reynolds number. In subsurface hydrology, porosities $\phi \approx 0.2-0.3$ are common; our sample has $\phi = 0.249$. To avoid confusion with the higher porosities ($\phi > 0.4$) often used in artificially created samples (Andrade Jr et al., 1999; Śnieżek et al., 2024) and in many geological application (Ghanbarian et al., 2023; Li et al., 2022; Lönartz et al., 2023), we refer to our sample as natural porous media. We explore how nonlinearity emerges in a complex, natural porous media. We numerically quantify and characterize these effects using detailed pore-scale simulations. Our results indicate that in the complex geological rock samples, the transition to inertial flows occurs via a distinct mechanism visible as a change in tortuosity and the early formation of vortical structures that evolve with inertial forces and change the structure, dispersion, and shape of preferential flow channels.

2. Methods

The reliability and accuracy of numerical simulations of the flow in porous media largely depend on the accuracy of the representation of the geometry of the actual granular medium. The size of the grains, their roughness, and the degree to which they fill the spaces in the rock directly affect the permeability of the rock and tortuosity of the

Figure 1. The slice of the intact clastic rock sample filled with synthetic resin (the photo of cross-sectional plane).

pore channels. A sample of intact clastic rock was taken during the field drilling operations. The pores of the sample were then filled with synthetic resin using a very slow process. Once the resin had hardened, thin slices of clastic rock were prepared from the cylindrical sample, representing different rock cross-sectional planes, and regular, high-resolution photos were taken (see Figure 1). Then, the two-dimensional pore map was extracted from a 2,794 × 3,999 resolution image with porosity $\phi = 0.249$.

For segmentation, we used image processing and created a binary map of pore space and obstacles using a scikit-image library (van der Walt et al., 2014), extracted clusters of grains using scikit-learn (Pedregosa et al., 2011), and Scipy (Virtanen et al., 2020). The clusters were then triangulated with Pyvista (Sullivan & Kaszynski, 2019) to produce geometry in STL format, which served as input for creating a computational domain that was discretized using the cfMesh utility (Juretić, 2015). Our approach generates a structured hexahedral mesh with local refinements in specific regions near the boundaries to increase accuracy.

The steady-state incompressible Navier-Stokes equations governed the fluid flow through the sample, and we solved them at the pore-scale level:

$$\nabla \cdot \mathbf{u} = 0, \quad \rho(\mathbf{u} \cdot \nabla \mathbf{u}) = -\nabla p + \mu \nabla^2 \mathbf{u} + \mathbf{f}, \tag{3}$$

where $\mathbf{u}$ is the velocity field, p is the pressure, $\rho\left[\mathrm{kg/m^3}\right]$ is the fluid density, $\mu[\mathrm{Pa \cdot s}]$ is the dynamic viscosity, and $\mathbf{f}$ is the body force. Note that the imposed body force f is equivalent to a constant pressure gradient via $\nabla p = -f$, which enforces a uniform driving force in the periodic domain and recovers Equation 1), (Fattahi et al., 2016; Matyka et al., 2008; Sivanesapillai et al., 2014). We used $\rho = 1$ and $\mu = 2 \cdot 10^{-6}$. We adopt the index notation for the components of vectors, namely, $\mathbf{u} \equiv [u_1, u_2]$, where index 1 corresponds to the horizontal component and index 2 corresponds to the vertical component. The computational domain was periodic in the streamwise (vertical) direction. It was created by mirroring the original sample to ensure continuity of the velocity and pressure fields across the domain and omitting the boundary effects known from channel experiments (Ko et al., 2023; Koponen et al., 1997). We solved Equation 3 in the entire domain, while the post-processing was done for various parameters in the original sample only.

The results were obtained using the standard finite-volume method implemented in OpenFOAMv. 2212 (Jasak et al., 2007). We used the steady-state simpleFoam solver, which utilizes pressure-velocity coupling and the Semi-Implicit Method for Pressure-Linked Equations (SIMPLE) algorithm (Patankar, 1980). Numerical steady-state solutions were obtained by ensuring all the residuals below 10^{-6}. Simulations were conducted in parallel on a 6-core processor using OpenMPI. To ensure numerical stability and convergence, we set the pressure under-relaxation to 0.6 and the velocity under-relaxation to 0.9, following established practices that offer a good trade-off between stability and solution accuracy (Jasak et al., 2007).

3. Results

The pore space is filled with fluid and subjected to an external body force to drive the flow. The force $\mathbf{f}$ starts from an extremely low value $\mathbf{f} = \left(0, -2 \times 10^{-15}\right)\left[\mathrm{kg/m^2\,s^2}\right]$ and increases, which results in changes in the Reynolds number, which is defined as $\mathrm{Re} = |\mathbf{U}| \cdot L/\nu$, where L is the width of the sample and $\mathbf{U}$ is the superficial velocity (Equation 1) and ν is the kinematic viscosity. Alongside of Re, we propose a pore-scale Reynolds number (Zeng & Grigg, 2006) $Re_p = |\mathbf{U}|\, \ell_h/\nu$, where $\ell_h = \frac{4A}{\ell_{sf}}[m]$ is a hydraulic length computed from the segmented pore map (with pore area $A = 1.54634 \times 10^7$, solid–fluid interfacial length $\ell_{sf} = 1.18939 \times 10^6$, consistent with computational units). For this fixed geometry, $\mathrm{Re} = \alpha\, Re_p$ with $\alpha = L/\ell_h \approx 53.7$ constant with $L = 2794\ [m]$, so all trends versus Re have an equivalent representation versus Re_p. The maximum Re was set to 10^3. Although local velocities in the narrow channels may yield a higher local Re, all SIMPLE runs remained numerically stable. The resulting velocity fields at two selected Reynolds numbers are shown in Figure 2. These results demonstrate the formation of a preferential channel at low Reynolds numbers (Figure 2, left), primarily

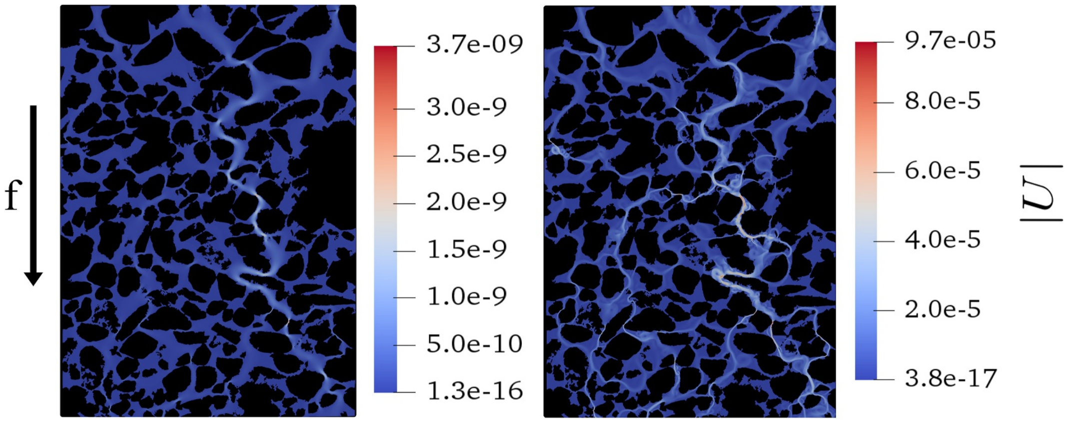

Figure 2. The magnitude of the pore-space velocity field at Re $= 0.03$ (left) and Re $= 9.62$ (right). The arrow indicates the direction of the body force driving the flow.

governed by viscous forces and increased momentum dispersion in high-Reynolds-flow (Figure 2, right), resulting in dispersed preferential channels where the maximum velocities are almost four orders of magnitude higher. A closer look at the flow field reveals that the vortex formation process is visible in the velocity field structure.

Next, we quantified the asymmetry in the velocity field by investigating the vorticity $\left(\omega = \frac{\partial u_2}{\partial x} - \frac{\partial u_1}{\partial y}\right)$ field over the entire computational domain (see Figure 3), which is divided into an upper (main) domain and its corresponding mirrored (buffer) domain. We compared the vorticity magnitudes at the corresponding nodes between these two regions. We defined the origin of the coordinate system at the bottom of the original sample. For each node $\mathbf{x_j} \equiv \left(x_j, y_j\right)$ in the upper (original) domain, we identified its mirror node $\mathbf{x}'_\mathbf{j} \equiv \left(x_j, 2H - y_j\right)$ in the lower (mirror) domain, where H is the size of one-half of the domain along the streamwise direction. Then, we calculated the sum of the absolute difference in vorticity magnitudes as

$$\Delta\omega = \sum_{j=1}^{N} \left| |\omega(\mathbf{x}_j)| - |\omega(\mathbf{x}'_j)| \right| \quad \text{with } \{\mathbf{x}_j\}_{j=1}^{N} = \Omega_U, \tag{4}$$

where Ω_U denotes the set of nodes in the upper domain. As shown in Figure 3, $\Delta\omega$ remained low at low Reynolds numbers, indicating that the flow remained symmetric in the Darcy regime. However, as the Reynolds number increases, the asymmetry of the flow field increases rapidly due to inertial effects. The main plot illustrates this transition, while the log-log inset confirms that the asymmetry grows monotonically across the entire range of Reynolds numbers, with a pronounced increase at relatively high Reynolds numbers. This increase in asymmetry highlights the emergence of complex flow structures. This suggests that factors other than pore geometry (symmetric in our case) play a crucial role in channel formation at high Re values.

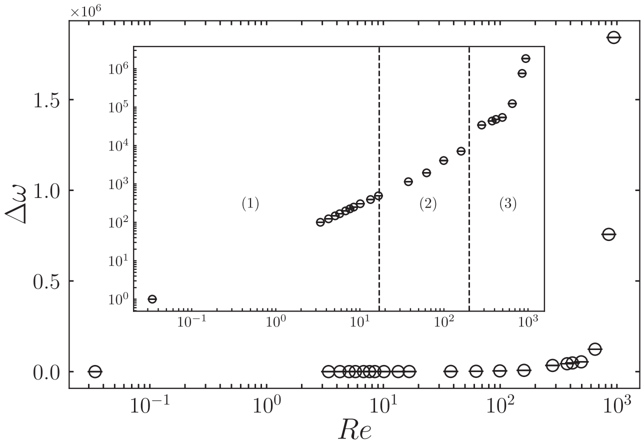

Figure 3. Mean values of $\Delta\omega$—the sum of the absolute difference in vorticity magnitude between the upper and lower halves of the domain—plotted versus Re, with vertical bars showing the full min–max range at each Re. The inset presents the same data on a log–log scale and highlights three regimes: (a) the power law ($\Delta\omega \propto \mathrm{Re}^p$), (b) slightly faster-than-exponential growth, and (c) a rapid "explosive" increase.

To assess the influence of inertia on the structure and its correlation with the asymmetry of the flow, we computed the friction factor (Andrade Jr et al., 1999) as follows:

$$\mathcal{F} = \frac{\mathbf{f}L}{\rho\langle|\mathbf{u}|\rangle^2}. \tag{5}$$

In a highly porous medium, the friction factor shows an apparent deviation at high velocities (Andrade Jr et al., 1999; Śnieżek et al., 2024) and indicates a transition from Darcy to nonlinear Forchheimer flows, where inertial forces

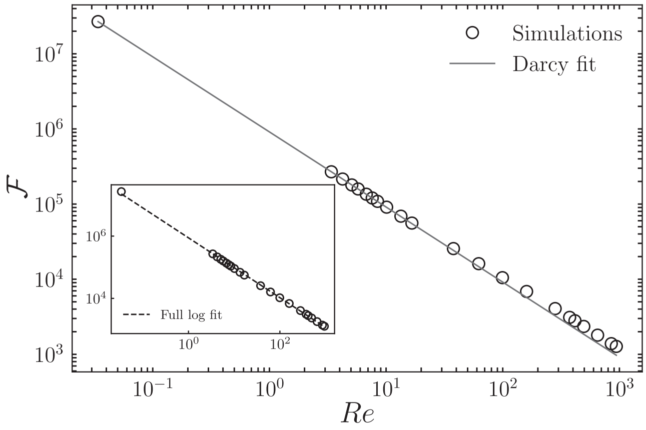

Figure 4. Generalized friction factor $\mathcal{F}$ versus $\log_{10}$ (Re), showing simulation data and a linear fit to the first four data points (solid line). The dashed line (inset) illustrates the full-range log-log fit.

become significant. However, in our simulations, this transition was not immediately evident (Figure 4). This is due to the low porosity and the dominant effect of the pore geometry guiding the flow through the system. We noticed that, if the numerical fit of Darcy, Equation 1 is taken over all data points, the friction factor follows the fit for the entire range of Reynolds numbers (see inset in Figure 4). Therefore, the flow at the highest Reynolds numbers may be mistakenly considered to lie in the Darcy regime.

To quantify the inertial effects visible in the velocity fields, as shown in Figure 2, we analyzed flow tortuosity τ

$$\tau = \frac{\langle |\mathbf{u}| \rangle}{\langle u_2 \rangle} \tag{6}$$

where $\langle u_2 \rangle$ is the average streamwise velocity component and $\langle |\mathbf{u}| \rangle$ is the average magnitude of the velocity. The notion of tortuosity was originally formulated based on purely geometrical factors like the length of the velocity field streamlines (Carman, 1997). Later, it was noted (Koponen et al., 1996) and formally proven (Duda et al., 2011) that in the absence of recirculation zones, the definition from Equation 6 is equivalent to taking the average of the normalized length of the streamlines weighted by each streamline's flux (Matyka et al., 2008). In our other work (Śnieżek et al., 2024) we used the definition from Equation 6 to quantify inertial effects in extremely high-porosity samples, and our further efforts are devoted to the deeper understanding of the behavior of this definition in flows with recirculation (Strzelczyk et al., 2025).

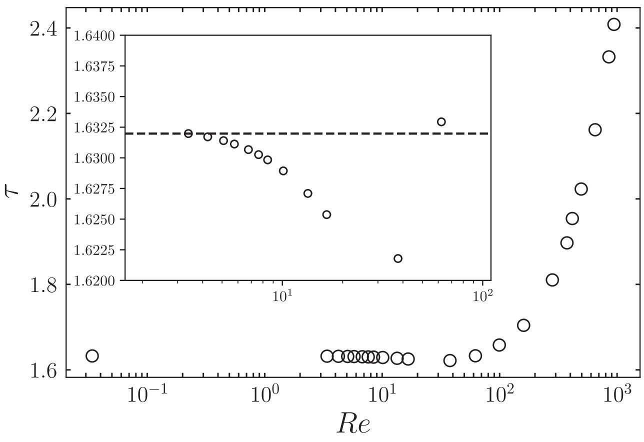

Figure 5. The tortuosity τ calculated using Equation 6 with increasing Re. The inset shows the first 14 data points, excluding the minimum Re.

Our results (Figure 5) indicate that the tortuosity remains constant at low Re and exhibits a relatively small decrease (see inset of Figure 5), reaching a minimum around Re = 30. This observation is consistent with our previously reported results for 3D, highly porous media (Śnieżek et al., 2024), where such a decrease in tortuosity is also noticeable. However, above this minimum, τ increases with Re, which has not been observed before. The non-monotonous rise of τ with Re suggests that the two competing mechanisms influence the tortuosity as the Reynolds number increases, and their relative importance depends on factors such as the flow speed, porosity, and geometric characteristics of the porous structure.

To understand the mechanism of the tortuosity changes, we investigated the fluid's kinetic energy distribution in the pore space. We calculated the participation number π, which quantifies the localization of kinetic energy distribution (Andrade Jr et al., 1999). It is defined as:

$$\pi \equiv \left(V \sum_{i=1}^{n} q_i^2 V_i \right)^{-1}, \tag{7}$$

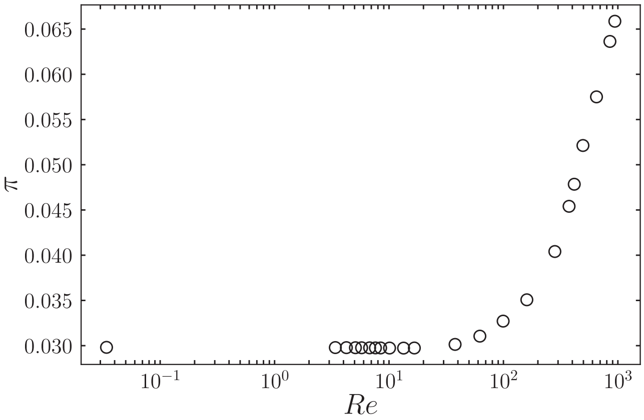

Figure 6. The growth of participation number π with Re.

where V_i is the volume of the i-th cell, and $q_i = \frac{e_i}{\sum_{j=1}^{n} e_j V_j}$ with $e_i \propto \boldsymbol{u}_i^2$ (Andrade Jr et al., 1999). The relationship between participation number and the Reynolds number is shown in Figure 6.

At low Reynolds numbers, π remains low and nearly constant, indicating the concentration of kinetic energy in a small fraction of pores and that we are in the Darcy regime. This is consistent with the visual inspection of the velocity field shown in Figure 2, where at a low Reynolds number, the flow is primarily through a single channel that emerges in the system. We find that π increases monotonically with Re, indicating that kinetic energy becomes more uniformly distributed across the pore space as inertial effects increase. This increase indicates that at high Re, the velocities outside the main channels and existing vortical cores increase even faster than those within them, revealing the formation of new flow pathways and a broader redistribution of kinetic energy. This behavior sheds more light on the tortuosity behavior shown in Figure 5, where the rapid rise may now be associated with an increasing number of vortices in the flow and the definition of tortuosity that was used. It is also notable that our results in the highly nonlinear regime, show $\pi \propto \tau$, which may be interesting to investigate in the future.

The steep rise in π is related to the reduction in preferential channeling accompanied by the emergence of vortices and flow recirculation zones in the pore space. To show this, we computed the parameter ρ^- (see Figure 7), introduced by us in (Śnieżek et al., 2024), which quantifies the volume fraction of the pore-space containing negative streamwise velocity. It is defined as:

$$\rho^- = \frac{1}{V} \sum_{i=1}^{n} f(u_{2,i})\, V_i, \tag{8}$$

where $u_{2,i}(\mathbf{r})$ is the streamwise velocity component, and V_i represents the volume of i-th cell. The function $f(u_2)$ is an indicator function defined as

$$f(u_2) = \begin{cases} 1, & u_2 < 0 \\ 0, & \text{otherwise.} \end{cases} \tag{9}$$

As shown in Figure 7, at low Reynolds numbers, ρ^- is not zero and is constant ($\rho^- \approx 0.24$), indicating the presence of flow reversal in the Darcy regime. We investigated this phenomenon (see Figures 8 and 9). We noticed that this occurs because of the combined effect of a small fraction of vortices appearing at the lowest Re and the dominant geometry-driven backward flow. In contrast, ρ^- investigated in a highly porous system (Śnieżek et al., 2024) was nearly 0 at a low Re.

The increase of ρ^- starts at about Re $= 3$ (see the inset of the left subplot of Figure 7) and coincides with the beginning of the decrease of τ in Figure 5. This indicates that the main mechanism behind the initial fall down of the currently studied tortuosity might be the growth of the recirculation zones in volume. As Re increases further, ρ^- rises rapidly around Re ≈ 10, earlier than the rise in τ is observed. The rise of ρ^- is non-monotonic, with local extrema visible for example, at Re ≈ 400. This fact, as well as the overall shape of $\rho^-(\text{Re})$ relation is compliant with the observations made in (Arbabi & Sahimi, 2024) concerning the volume of the recirculation zones (compare the right subplot of Figures 7 and 9 in Arbabi & Sahimi, 2024). It suggests that in the studied sample numerous local reorganizations of velocity field take place at higher Re.

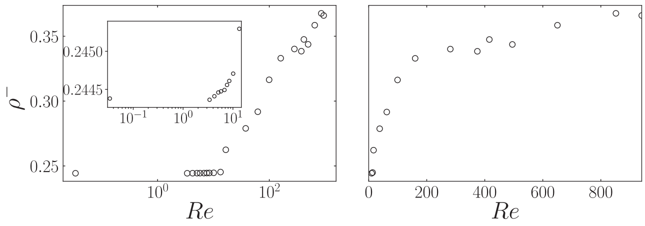

Figure 7. ρ^- versus Re. All the plots show the same data. The left subplot is the lin-log plot in the whole range of Re, its inset shows the magnification of Re < 13 range. The right subplot uses linear scales on both axes.

Our analysis of ρ^- (Figure 7) suggest that vortices appear earlier than significant changes in tortuosity and before a substantial increase in the energy

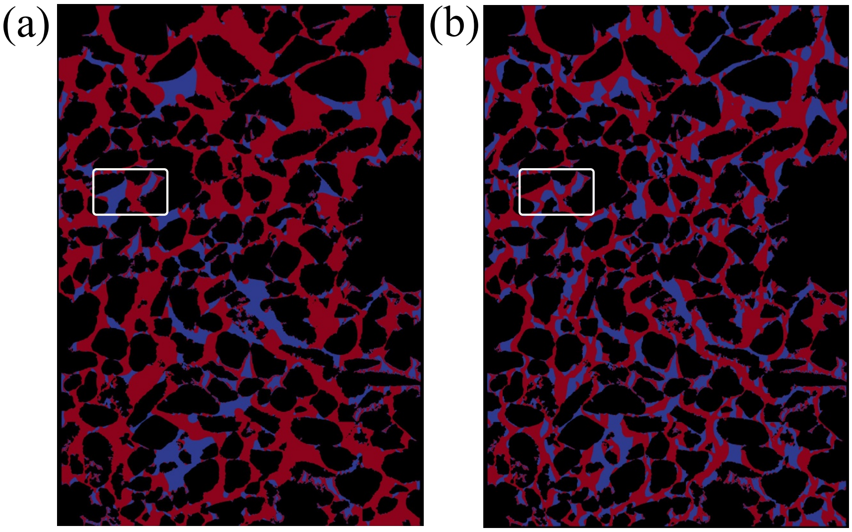

Figure 8. The maps of $f(u_2)$ (Equation 9) for (a) $\mathrm{Re} = 0.03$, and (b) $\mathrm{Re} = 940.94$. Red (dark in grayscale) indicates $f(u_2) = 1$, whereas blue (light in grayscale) indicates $f(u_2) = 0$. The white frame in each plot indicates the areas shown at the magnification in Figure 8.

distribution. To understand this and describe the physical mechanism behind the ρ^- increase, we visualized the spatial map distribution of the backward-flow indicator $f(u_2)$. This highlights the regions of reverse flow within the pore space (Figure 8, and zoomed regions in Figure 9 for two representative Reynolds numbers). Surprisingly, at a low Reynolds number ($\mathrm{Re} = 0.03$), isolated flow pockets of non-zero ρ^- appear and confirm the presence of

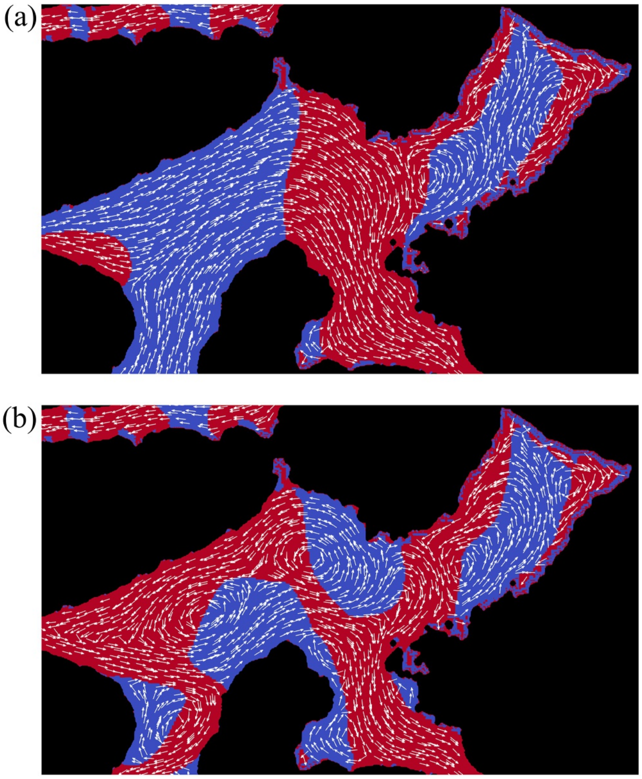

Figure 9. The magnification of particular regions of the maps of $f(u_2)$ (Equation 9) as shown in Figure 8. Vectors represent the local direction of the velocity field. For clarity, vectors close to the solid boundaries are omitted.

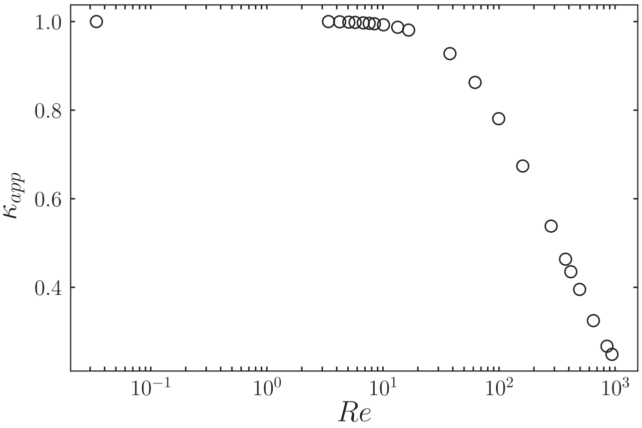

Figure 10. The normalized apparent permeability κ_{app} versus Re.

backward flow and localized vortices. As the Reynolds number increased, the reverse-flow regions shrank in favor of the dominant vortex component (Figure 8, right panel), forming numerous neighboring recirculation zones. For a relatively high Re $= 940.94$, a complex and widely dispersed vortex structure system was visible throughout the entire pore space. The extensive, more dispersed backward flow regions, now in high Re, visible primarily as vortices, correlate with the sharp rise in ρ^{-} observed in Figure 7, as well as the increasing trends in τ and ϕ.

To quantify this, we fitted the power law $\kappa_{\text{app}} \propto \tau^{-b}$ and found $b \approx 1/3$ (see Figure 11). This behavior aligns with the results of the impact of tortuosity on permeability in the flow observed in the Darcy regime for systems of varying porosities reported previously (Koponen et al., 1997). Intriguingly, in the inertial regime, the appearance of vortices accelerates the flow in narrower, more tortuous channels, effectively accelerating the macroscopic flow by reducing shear stresses along the pore walls. However, this process still leads to a net decrease in apparent permeability (see Figure 10).

4. Conclusions

We have shown that natural porous media at relatively low-porosity exhibit a different transition mechanism from a low Reynolds number (Darcy flow) to a high Reynolds number (non-Darcy flow) if compared to a highly porous medium (Śnieżek et al., 2024). By studying the spatial structure of the velocity in pore-space we found that the complex structures of the pore geometry led to the emergence of vortices even at low Reynolds numbers. Moreover, the deeper study of ρ^{-} indicates the backward flow induced by geometry. To understand this, we investigated tortuosity and observed its non-monotonic growth. We associate this with two physical mechanisms: straightening the flow streamlines due to increased momentum localized in the channels with a more dispersed flow structure in general (lowering τ), and the appearance of vortices (increasing τ). We found, that pore-scale indicators—ρ^{-}, τ, and π capture the onset and evolution of inertia even when the generalized friction factor remains nearly linear. Our study shows, that increase in tortuosity, driven by inertial effects in the flow results in apparent permeability drop. Finally, we compared the tortuosity with the apparent permeability and determined the power law $\kappa_{\text{app}} \propto \tau^{-1/3}$ that holds in the inertial regime.

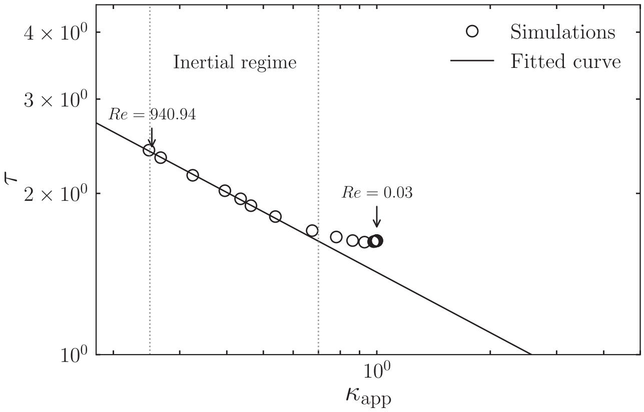

Figure 11. Correlation between tortuosity τ and the apparent permeability κ_{app} measured in the flow. The numerical fit of the power law relation was taken in the inertial regime and drawn as a solid line. The dashed lines guide the eye to distinguish the inertial regime of the flow roughly.

Conflict of Interest

The authors declare no conflicts of interest relevant to this study.

Data Availability Statement

Numerical results, simulated velocity fields, and code script supporting this study are openly available on Zenodo under a Creative Commons Attribution (CC BY 4.0) license at (Naqvi & Matyka, 2025). The repository contains: (a) pore-space geometry and mesh files (STL and .fms for OpenFOAM case), (b) steady laminar pore-scale simulations configured for OpenFOAM v2212 (simpleFoam) with all dictionaries and run scripts, (c) VTK outputs across the studied Reynolds-number range, and (d) post-processing data of tortuosity τ, participation number π, backward-flow fraction ρ^{-}, friction factor $\mathcal{F}$, and apparent permeability κ_{app}.

Acknowledgments

We are grateful to Josè S. Andrade Jr. for insightful discussion and comments during the early stages of the work. Funded by National Science Centre, Poland under the OPUS call in the Weave programme 2021/43/I/ST3/00228. This research was funded in whole or in part by National Science Centre (2021/43/I/ST3/00228). For the purpose of Open Access, the author has applied a CC-BY public copyright licence to any Author Accepted Manuscript (AAM) version arising from this submission. M. Matyka acknowledges the financial support from the Slovenian Research And Innovation Agency (ARIS) research core funding No. P2-0095.

References

Arbabi, S., & Sahimi, M. (2024). The transition from Darcy to nonlinear flow in heterogeneous porous media: I—Single-phase flow. *Transport in Porous Media*, *151*(4), 795–812. https://doi.org/10.1007/s11242-024-02070-3

Arthur, J. (2020). PIV study of flow through and over porous media at the onset of inertia. *Advances in Water Resources*, *146*, 103793. https://doi.org/10.1016/j.advwatres.2020.103793

Banerjee, A., & Paul, D. (2021). Developments and applications of porous medium combustion: A recent review. *Energy*, *221*, 119868. https://doi.org/10.1016/j.energy.2021.119868

Basak, P. (1977). Non-Darcy flow and its implications to seepage problems. *Journal of the Irrigation and Drainage Division*, *103*(4), 459–473. https://doi.org/10.1061/jrcea4.0001172

Cao, S. C., Jung, J., & Radonjic, M. (2019). Application of microfluidic pore models for flow, transport, and reaction in geological porous media: From a single test bed to multifunction real-time analysis tool. *Microsystem Technologies*, *25*(11), 4035–4052. https://doi.org/10.1007/s00542-019-04612-y

Carman, P. (1997). Fluid flow through granular beds. *Chemical Engineering Research and Design*, *75*, S32–S48. https://doi.org/10.1016/S0263-8762(97)80003-2

Darcy, H. (1856). *Les Fontaines Publiques de la Ville de Dijon*. Victor Dalmont.

Duda, A., Koza, Z., & Matyka, M. (2011). Hydraulic tortuosity in arbitrary porous media flow. *Physical Review E: Statistical, Nonlinear, and Soft Matter Physics*, *84*(3), 036319. https://doi.org/10.1103/physreve.84.036319

Fattahi, E., Waluga, C., Wohlmuth, B., Rüde, U., Manhart, M., & Helmig, R. (2016). Lattice Boltzmann methods in porous media simulations: From laminar to turbulent flow. *Computers and Fluids*, *140*, 247–259. https://doi.org/10.1016/j.compfluid.2016.10.007

Forchheimer, P. (1901). Wasserbewegung Durch den Boden. *Zeitschrift des Vereines Deutscher Ingenieure*, *45*, 1781–1788.

Fourar, M., Lenormand, R., Karimi-Fard, M., & Horne, R. (2005). Inertia effects in high-rate flow through heterogeneous porous media. *Transport in Porous Media*, *60*(3), 353–370. https://doi.org/10.1007/s11242-004-6800-6

Ghanbarian, B., Mehmani, Y., & Berkowitz, B. (2023). Effect of pore-wall roughness and Péclet number on conservative solute transport in saturated porous media. *Water Resources Research*, *59*(2), e2022WR033119. https://doi.org/10.1029/2022wr033119

Hovorka, S. C., Treviño, R. H., Nicot, M. J., et al. (2019). Dynamic processes of co storage in the field: 1. Multiscale and multiphase flow behavior. *Water Resources Research*, *55*(1), 1–17. https://doi.org/10.1029/2019WR025688

Hyman, J. D. (2020). Flow channeling in fracture networks: Characterizing the effect of density on preferential flow path formation. *Water Resources Research*, *56*(9), e2020WR027986. https://doi.org/10.1029/2020wr027986

Jasak, H., Jemcov, A., Tukovic, Z., et al. (2007). Openfoam: A C++ library for complex physics simulations. *International workshop on coupled methods in numerical dynamics*, *1000*, 1–20.

Jr Andrade, J., Costa, U., Almeida, M., Makse, H., & Stanley, H. (1999). Inertial effects on fluid flow through disordered porous media. *Physical Review Letters*, *82*(26), 5249–5252. https://doi.org/10.1103/physrevlett.82.5249

Juretić, F. (2015). cfMesh user guide. *Computer software manual]. Zagreb*. https://cfmesh.com/documentation/

Ko, D., Ji, H., & Ju, Y. S. (2023). Prediction of 3D velocity field of reticulated foams using deep learning for transport analysis. *Transport in Porous Media*, *148*(3), 577–604. https://doi.org/10.1007/s11242-023-01961-1

Koponen, A., Kataja, M., & Timonen, J. (1996). Tortuous flow in porous media. *Physical Review E—Statistical Physics, Plasmas, Fluids, and Related Interdisciplinary Topics*, *54*(1), 406–410. https://doi.org/10.1103/PhysRevE.54.406

Koponen, A., Kataja, M., & Timonen, J. (1997). Permeability and effective porosity of porous media. *Physical Review E*, *56*(3), 3319–3325. https://doi.org/10.1103/physreve.56.3319

Li, H., Michael, H. A., & Wilson, A. M. (2022). Coupled effects of density and dual-domain mass transfer on aquifer storage and recovery. *Water Resources Research*, *58*(6), e2021WR031445. https://doi.org/10.1029/2021WR031445

Lönartz, M., Neuweiler, I., Bechtold, M., Bosbach, D., & Poonoosamy, J. (2023). Capturing the dynamic processes of porosity clogging in porous media: A pore-network modeling study. *Water Resources Research*, *59*(6), e2023WR034722. https://doi.org/10.1029/2023WR034722

Matyka, M., Khalili, A., & Koza, Z. (2008). Tortuosity-porosity relation in porous media flow. *Physical Review E*, *78*(2), 026306. https://doi.org/10.1103/physreve.78.026306

Matyka, M., & Mądrala, M. (2017). Granica laminarnego przepływu wody w obsypce żwirowej studni eksploatacyjnej. *Przeglad Geologiczny*, *65*(11/2), 1334–1338.

Muljadi, B. P., Blunt, M. J., Raeini, A. Q., & Bijeljic, B. (2015). *The impact of porous media heterogeneity on non-Darcy flow behaviour. Adv*. Water Res.

Muljadi, B. P., Blunt, M. J., Raeini, A. Q., & Bijeljic, B. (2016). The impact of porous media heterogeneity on non-Darcy flow behaviour from pore-scale simulation. *Advances in Water Resources*, *95*, 329–340. https://doi.org/10.1016/j.advwatres.2015.05.019

Naqvi, S. B., & Matyka, M. (2025). Data: Inertial effects on fluid flow through natural porous media. *Zenodo*. https://doi.org/10.5281/zenodo.17161579

Neuman, S. P. (1977). Theoretical derivation of Darcy's law. *Acta Mechanica*, *25*(3–4), 153–170. https://doi.org/10.1007/bf01376989

Nissan, A., & Berkowitz, B. (2018). Inertial effects on flow and transport in heterogeneous porous media. *Physical Review Letters*, *120*(5), 054504. https://doi.org/10.1103/physrevlett.120.054504

Patankar, S. V. (1980). *Numerical heat transfer and fluid flow*. Hemisphere Publishing Corporation.

Pedregosa, F., Varoquaux, G., Gramfort, A., Michel, V., Thirion, B., Grisel, O., et al. (2011). Scikit-learn: Machine learning in Python. *Journal of Machine Learning Research*, *12*, 2825–2830.

Sivanesapillai, R., Steeb, H., & Hartmaier, A. (2014). Transition of effective hydraulic properties from low to high Reynolds number flow in porous media. *Geophysical Research Letters*, *41*(14), 4920–4928. https://doi.org/10.1002/2014gl060232

Śnieżek, D., Naqvi, S. B., & Matyka, M. (2024). Inertia onset in disordered porous media flow. *Physical Review E*, *110*(4), 045103. https://doi.org/10.1103/physreve.110.045103

Strzelczyk, D., Kosec, G., & Matyka, M. (2025). The role of porosity in the transition to inertial regime in porous media flows. (in preparation).

Sullivan, C. B., & Kaszynski, A. (2019). PyVista: 3d plotting and mesh analysis through a streamlined interface for the visualization toolkit (VTK). *Journal of Open Source Software*, *4*(37), 1450. https://doi.org/10.21105/joss.01450

van der Walt, S., Schönberger, J. L., Nunez-Iglesias, J., Boulogne, F., Warner, J. D., Yager, N., & the scikit-image contributors. (2014). scikit-image: Image processing in Python. *PeerJ*, *2*, e453. https://doi.org/10.7717/peerj.453

Virtanen, P., Gommers, R., Oliphant, T. E., Haberland, M., Reddy, T., Cournapeau, D., & SciPy 1.0 Contributors. (2020). SciPy 1.0: Fundamental algorithms for scientific computing in python. *Nature Methods*, *17*(3), 261–272. https://doi.org/10.1038/s41592-019-0686-2

Wang, F., Shuai, Y., Wang, Z., Leng, Y., & Tan, H. (2014). Thermal and chemical reaction performance analyses of steam methane reforming in porous media solar thermochemical reactor. *International Journal of Hydrogen Energy*, *39*(2), 718–730. https://doi.org/10.1016/j.ijhydene.2013.10.132

Wang, L., Li, Y., Zhao, G., Chen, N., & Xu, Y. (2019). Experimental investigation of flow characteristics in porous media at low Reynolds numbers (re→ 0) under different constant hydraulic heads. *Water*, *11*(11), 2317. https://doi.org/10.3390/w11112317

Whitaker, S. (1986). Flow in porous media i: A theoretical derivation of Darcy's law. *Transport in Porous Media*, *1*(1), 3–25. https://doi.org/10.1007/BF01036523

Whitaker, S. (1996). The forchheimer equation: A theoretical development. *Transport in Porous Media*, *25*(1), 27–61. https://doi.org/10.1007/bf00141261

Zeng, Z., & Grigg, R. (2006). A criterion for non-Darcy flow in porous media. *Transport in Porous Media*, *63*(1), 57–69. https://doi.org/10.1007/s11242-005-2720-3

Zhang, Y., Zhou, Y., Zhang, Y., Zhang, Z., Liu, J., Zhu, J., et al. (2024). Optimal design of silver-loaded zeolite filter structure based on porous media model. *Separation and Purification Technology*, *334*, 125905. https://doi.org/10.1016/j.seppur.2023.125905